Chapter 3.2

X-ray Absorption Fine Structure Spectroscopy

K. I. Pandya and **D. C. Koningsberger**
Department of Chemical Technology, Laboratory for Inorganic Chemistry and Catalysis, University of Eindhoven, 5600 MB Eindhoven, The Netherlands

List of Symbols

$A_j(k)$	Amplitude of EXAFS for the jth coordination shell as a function of k
$A_r(k)$	Amplitude of EXAFS for reference absorber–back-scatter pair
$A_s(k)$	Amplitude of EXAFS for unknown compound
c	Speed of light
e	Charge of electron
h	Planck constant
$\hbar$	Planck constant divided by 2π
E	Energy of the X-ray photons
E_b	Binding energy of a core electron in the absorber atom
E_f	Final state energy of the photoelectron
E_k	Kinetic energy of the ejected photoelectron
$\mathbf{E}$	Electric field polarization vector of the X-ray photons
$F(k)$	Back-scattering amplitude of neighbour atoms around the absorber atom; subscripts j, r and s have the same meaning as for $A(k)$
I	Intensity of transmitted X-ray beam
I_0	Intensity of incident X-ray beam
I_f	Intensity of fluorescence photons
k	Wave vector of the ejected photoelectron
m	Mass of electron
N_j	Coordination number of jth shell; subscripts r and s have the same meaning as for $A(k)$
R_j	Distance between the absorber atom and back-scattering atoms of jth shell; subscripts r and s have the same meaning as for $A(k)$

Analysis of Microelectronic Materials and Devices. Edited by M. Grasserbauer and H. W. Werner

x Sample thickness
λ Wavelength of the photoelectron
$\lambda(k)$ Mean free path of the photoelectron as a function of k; subscripts j, r and s have the same meaning as for $A(K)$
$\mu(E)$ X-ray absorption coefficient of an absorber as a function of photon energy
$\mu_0(E)$ X-ray absorption coefficient of an isolated absorber without any back-scatterers
ν Frequency of the X-ray photon
$\rho(E_f)$ Density of allowed states at the final state energy E_f
σ_j Deviation in R_j caused by static and thermal disorder of the back-scatterer atoms in j shell
$\Delta\sigma_j^2$ Debye–Waller factor; deviation of σ^2 with respect to the reference compound
$\phi(k)$ Phase shift suffered by the photoelectron in the scattering process; subscripts j, r and s have the same meaning as for $A(k)$
$\Phi(k)$ The argument of the sin term in equation (7); subscripts j, r and s have the same meaning as for $A(k)$
$\chi(k)$ The EXAFS function
$\psi_i(k)$ Initial state wave function of a core electron
$\psi_f(k)$ Final state wave function of the ejected photoelectron
ω Angular frequency of X-ray photon

3.2.1 Introduction

A fundamental problem of science is the structural and electronic characterization of a material which provides basic understanding of its properties. Traditionally, diffraction techniques (XRD, neutron diffraction, LEED) have been used for most of the structural investigations and reliable structures can be determined for materials that exhibit a long-range structural order. The structures of highly disordered solids and amorphous materials can not be determined by diffraction techniques.

X-ray absorption fine structure (XAFS) spectroscopy is a powerful technique to characterize all forms of matter irrespective of their degree of crystallinity. The extended X-ray absorption fine-structure (EXAFS) spectroscopy probes the local structure of the material [1]. In addition, the chemical state and the local electronic structure of the absorber atom can be determined from the X-ray absorption near edge structure (XANES) spectroscopy within about 40 eV of the X-ray absorption edge [2]. One of the major advantages of XAFS is its atomic selectivity which enables a user to investigate the local structure of each different constituent of a sample. The recent availability of high-brightness synchrotron radiation sources has resulted in a prosperous development of XAFS spectroscopy.

The present chapter furnishes a brief discussion of the concepts of XAFS followed by some illustrations of the use of this technique for studying the structure of a few selected systems.

3.2.2 Theory of XAFS

3.2.2.1 General principle

An XAFS experiment simply requires an accurate determination of the X-ray absorption coefficient μ of a material as a function of the X-ray photon energy. When a monochromatic X-ray beam passes through a medium, its intensity is attenuated exponentially according to the relation

$$I = I_0 \exp\{-\mu(E)x\} \tag{1}$$

where I_0 is the intensity of the incident photons, I is the intensity of the transmitted photons, x is the thickness of the sample and E is the energy of the X-ray photons. Figure 1 shows the X-ray absorption spectrum of a 7 μm thick nickel foil. The initial monotonically decreasing part of the spectrum is due to the interaction of X-rays with the outer shell electrons, and can be described by equation (1). When the X-ray energy $h\nu$ is equal to or greater than the binding energy E_b(E_b = 8333 eV for nickel K shell) of a core level, the bound electron is emitted by the photoelectric process and a sharp increase in the absorption spectrum is observed. This is called the absorption edge and it is a characteristic of the absorber atom. For photon energies greater than the binding energy, the absorption coefficient shows a series of oscillations which may extend up to 2000 eV above an absorption edge. The fine structure in the energy range close to the absorption edge (-10 eV $< E - E_b <$ $+40$ eV) (XANES) contains information about the local electronic structure and geometrical configuration of the material. The oscillations from about 40 eV above the absorption edge are called EXAFS and they contain information about the local structure around the excited atom. The origin of the fine structure is outlined below.

In the photoelectric process, the energy of an X-ray photon is completely absorbed by a core electron, which in turn is promoted to an unoccupied valence level or to the continuum. The kinetic energy E_k of the emitted photoelectron is

$$E_k = h\nu - E_b \tag{2}$$

Quantum mechanically, the ejected photoelectron can be viewed as an outgoing spherical wave with wavelength λ defined as

$$\lambda = \frac{2\pi}{k} \tag{3}$$

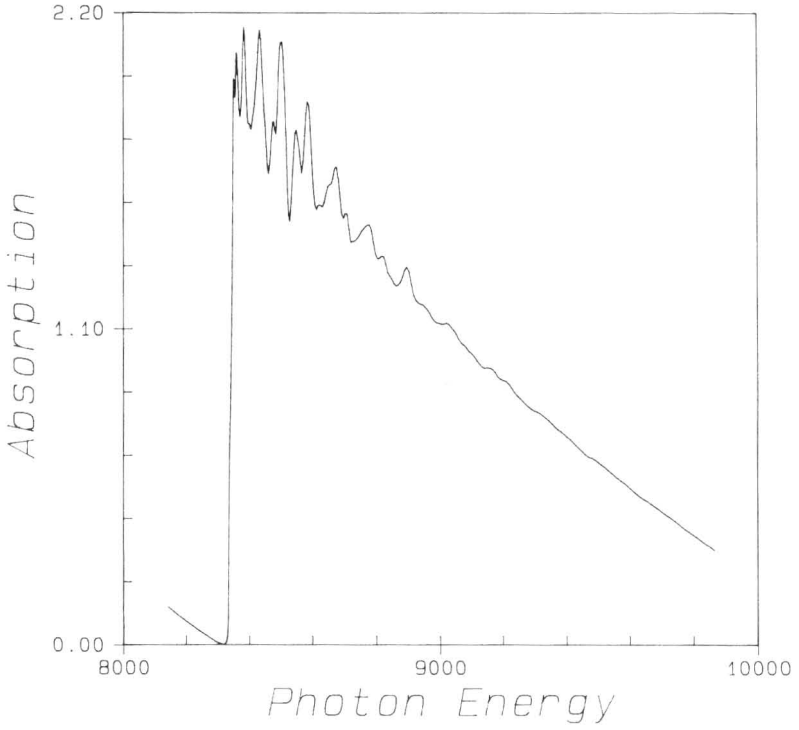

Figure 1 X-ray absorption spectrum of a 7 μm thick nickel foil measured at 77 K on beamline X-11A of the National Synchrotron Light Source, Brookhaven (USA)

where k is the photoelectron wave vector given by

$$k = \left[\left(\frac{2m}{\hbar^2}\right)(h\nu - E_b)\right]^{1/2} \tag{4}$$

Here m is the electron mass and $\hbar$ is Planck's constant divided by 2π. In dipole approximation the probability of photoelectric absorption for a K-shell electron is given by

$$P = \frac{2\pi^2 e^2}{\omega c^2 m} | < \psi_f | \mathbf{E}.\mathbf{r} | \psi_i > |^2 \rho(E_f) \tag{5}$$

where ψ_i is the initial state wave function of the bound electron, ψ_f is the final state wave function of the ejected photoelectron and $\rho(E_f)$ is the density of the allowed states at the final state energy E_f. $\mathbf{E}$ is the electric field polarization vector of the X-ray photons, $\mathbf{r}$ is the position vector of the scatterer with respect to the absorber atom, e is the electronic charge, ω is the angular frequency of the photon and c is the speed of light. For an isolated atom, μ

decreases smoothly at energies above the edge energy and does not show fine structure. This is the case for a monoatomic gas such as krypton. However, when the absorbing atom is surrounded by other atoms, as in a molecular gas or any condensed phase, the outgoing photoelectron wave is backscattered by the surrounding atoms, as shown in Figure 2. Hence the final state wave function $|\psi_f>$ has two contributions, $|\psi_f>_{outgoing}$ and $|\psi_f>_{backscattered}$. The backscattered part of the wave interferes with the outgoing part creating an interference pattern. As the photon energy changes, the energy and thus the wavelength of the ejected photoelectron changes, causing constructive or destructive interference at the absorber atom. This interference modulates the

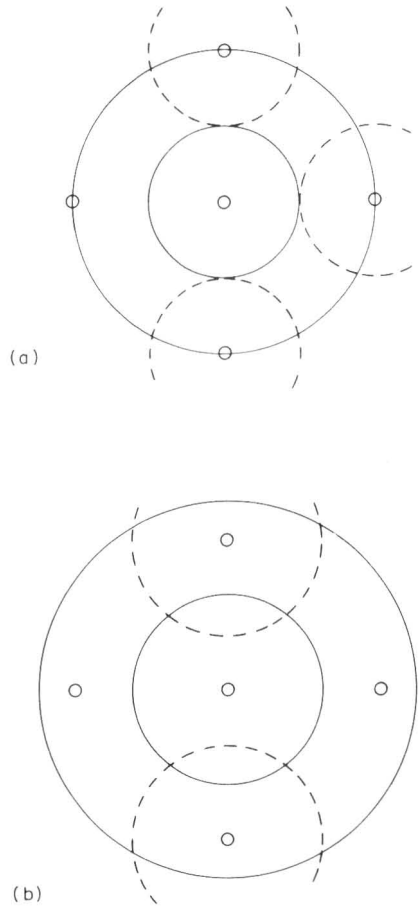

Figure 2 A schematic representation of the EXAFS process. The outgoing and the back-scattered waves interfere (a) constructively and (b) destructively at the absorber atom

final state wave function $|\psi_f>$ and thus the transition probability (see equation 5) of reaching this final state. Since the absorption coefficient μ is proportional to the transition probability, μ is modulated by the interference pattern as well. In Figure 2(a) the amplitude of the outgoing and the back-scattered wave interfere constructively, leading to a maximum in the absorption coefficient, while in Figure 2(b) the amplitudes interfere destructively, resulting in a minimum in the absorption coefficient.

The absorption coefficient above the absorption edge is defined as

$$\mu(k) = \mu_0(k)\{1 + \chi(k)\} \tag{6}$$

where $\mu_0(k)$ represents the smooth varying (atomic) background and $\chi(k)$ represents the oscillatory part of the total absorption coefficient $\mu(k)$. Since the oscillations are based upon the interference between the outgoing and scattered wave from the neighbour atoms and since this interference is determined by the local atomic configuration, the fine structure contains information about the local structure around the ionized atoms. In general, the amplitude and the phase of the fine structure contain information about the coordination number, bond distances and local disorder, respectively.

3.2.2.2 Principles of EXAFS

A simple way of deriving the EXAFS equation is by considering the one-electron single scattering model in plane wave approximation where the ejected photoelectron is assumed to scatter only once before it returns to the absorber atom. With this approximation the EXAFS oscillations can be described by the sum of sine waves originating from all the shells of neighbouring atoms [4, 5]:

$$\chi(k) = \sum_j A_j(k)\sin\{\Phi_j(k)\} \tag{7}$$

with

$$\Phi_j = 2kR_j + \phi_j(k) \tag{7a}$$

Here j refers to the jth coordination shell, R_j is the average interatomic distance between the absorber atom and the neighbouring atoms in the jth shell and $\phi_j(k)$ is the phase shift experienced by the electron in the scattering process. $A_j(k)$ is the amplitude function which is expressed as:

$$A_j(k) = \frac{N_j}{kR_j^2} S_0^2 F_j(k) e^{-2R_j/\lambda(k)} e^{-\sigma_j^2 k^2} \tag{7b}$$

where N_j is the average coordination number in the jth shell and σ_j^2 is a Debye–Waller type of term which represents the root mean square fluctuation in R_j caused by thermal motion of the atoms and the structural disorder

present in the material, $F_j(k)$ is the back-scattering amplitude and reflects the scattering power of the neighbouring atoms, the exponential term $e^{-2R_j/\lambda(k)}$ accounts for the finite lifetime of the excited state and $S_0^2(k)$ is an amplitude reduction factor which accounts for the photoelectron energy loss due to many body effects and shake-up/shake-off processes in the absorber atom.

3.2.2.3 Principles of XANES

The structure in the vicinity of an absorption edge constitutes a XANES spectrum. Near the absorption edge, the mean free path λ of the photoelectron

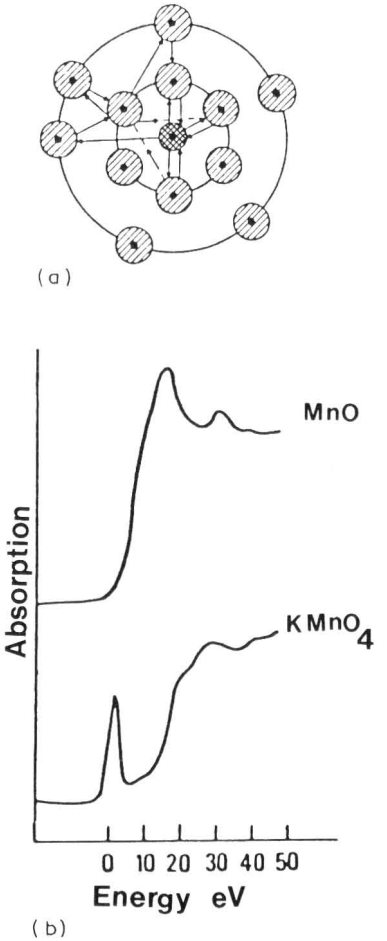

Figure 3 (a) Multiple scattering processes for the low-energy photoelectron. (b) Mn K-edge XANES spectra of MnO (octahedral) and $KMnO_4$ (tetrahedral)

is very large and suffers multiple scattering before returning to the absorber atom [2] (Figure 3a). Hence the one-electron single scattering model assumed for EXAFS is not valid for XANES. The edge structure is primarily caused by the transition of the core electron to empty electronic states of the material. There are a variety of phenomena contributing to a XANES spectrum, but, in principle, it can be viewed in terms of (a) electronic states and (b) multiple scattering. Both of the approaches are equivalent since the geometrical structure and the electronic structure are closely related to each other.

The XANES spectra contain information about the coordination geometry (bond angles), symmetry of unoccupied states and effective atomic charge on the absorbing atom [6, 7]. There are many physical phenomena that contribute to XANES. For metals and semiconductors, features arising from core excitations, many-body effects and partial density of states are found in the XANES spectra. For molecular samples, Rydberg and valence states, multiple scattering resonances (MSR) and shake-up peaks constitute XANES. As a result, the interpretation of XANES is not simple and one must rely upon theoretical calculations. A detailed theoretical aspect of XANES is beyond the scope of this book and we advise the reader to look at excellent recent reviews [2, 7].

An example of how XANES can be used may be illustrated by comparing XANES spectra of tetrahedrally and octahedrally coordinated transition metal complexes. Figure 3(b) shows manganese K-edge XANES spectra of MnO_2 and $KMnO_4$. The pre-edge peak seen below the main absorption edge arises from a $1s \rightarrow 3d$ transition. The existence and intensity of the pre-edge peak is determined by the symmetry of the metal–ligand bond. For tetrahedral complexes, the lack of a centre of symmetry permits a dipole transition from 1s to 3d, giving rise to a strong pre-edge peak as observed for $KMnO_4$. For purely octahedrally coordinated systems (with a centre of symmetry) such as MnO, the dipole transition is forbidden, so no pre-edge peak is observed.

3.2.3 Data Analysis

In this section the XAFS data analysis procedure is described briefly. For a detailed discussion, readers are referred to recent reviews [8–10].

The first step in the analyses of an XAFS spectrum is to separate the XAFS oscillations from the experimentally measured X-ray absorption coefficient μx. The raw XAFS spectrum for a nickel foil is shown in Figure 4(a).

A standard procedure to remove the pre-edge absorption involves fitting the spectrum in the energy range sufficiently below the absorption edge (typically -200 to -40 eV) with a polynomial. The fitted polynomial is extrapolated past the edge and subtracted from the entire spectrum. This step removes the absorption due to all other electrons and isolates the K-shell (for nickel) contribution to the total absorption.

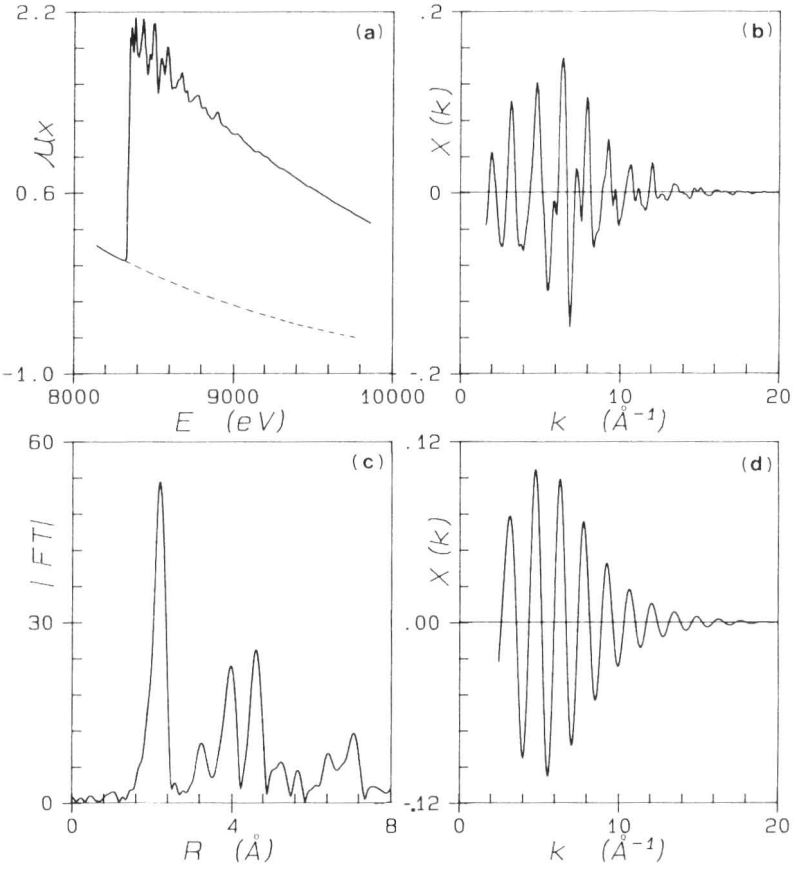

Figure 4 (a) X-ray absorption spectrum of a 7 μm thick nickel foil. The pre-edge background is shown by the dotted line. (b) The normalized EXAFS function plotted as $\chi(k)$ versus k for the nickel foil. (c) Fourier transform of the EXAFS data shown in (b). (d) The isolated EXAFS function for the first shell of nickel foil obtained by inverse Fourier transformation

For EXAFS data analysis the smoothly varying post-edge background μ_0 is removed by fitting the post-edge region (typically starting at 30 eV above the edge) with a spline function and subtracting it from the data. The criterion for an adequate background removal is that in the first derivative of the calculated background the EXAFS oscillations just begin to appear. The EXAFS function is then normalized on a per atom basis by dividing the data through the edge jump $\Delta\mu_0 x$ at the absorption edge. The normalized EXAFS function is converted to k-space by using equation (4). In the initial stage of analysis, the value of E_b is chosen at the maximum derivative point on the edge. At

later stages, E_b is varied and adjusted to its proper value. The normalized EXAFS spectrum for the nickel foil is shown in Figure 4(b).

The EXAFS function shown in Figure 4(b) is superposition of an unknown number of coordination shells. Fourier transformation of $\chi(k)$ yields peaks in r-space corresponding to individual coordination shells around the absorbing atom. These peaks are shifted to lower r-values from the real interatomic distances due to the influence of the phase shift function. The Fourier transform of the nickel foil EXAFS spectrum is shown in Figure 4(c).

The EXAFS function of a particular coordination shell can be isolated by applying a window in r-space and performing an inverse Fourier transform to k-space. This step produces a modulated sinusoidal function with amplitude $A_j(k)$ and argument $\Phi_j(k)$, as given in equation (7). The isolated EXAFS function for the first shell of nickel foil is shown in Figure 4(d). The information about N, σ^2 and R can now be obtained if $F(k)$, $\lambda(k)$, $S_0^2(k)$ and $\phi(k)$ are known. These factors can be derived from the EXAFS measurements on a reference sample (designated by subscript r) of known structure having an identical absorber–scatterer pair as in the unknown sample (designated by subscript s) and assuming that $\phi(k)$ and $F(k)$ are transferable from the reference compound to the unknown sample. This is known as the phase and amplitude transferability which is given by

$$\phi_r(k) = \phi_s(k), \qquad F_r(k) = F_s(k) \qquad \lambda_r(k) = \lambda_s(k), \qquad S_{0r}^2 = S_{0s}^2 \tag{8}$$

Comparing the argument of sine functions of the sample and the reference compound,

$$\Phi_s(k) - \Phi_r(k) = 2k(R_s - R_r) \tag{9}$$

The unknown distance R_s can be determined. A minor adjustment for E_b is needed to account for the difference in the edge position between the two samples. Knowing R_s and comparing the amplitudes $A_s(k)$ and $A_r(k)$,

$$\frac{A_r(k)}{A_s(k)} = \frac{N_r R_s^2}{N_s R_r^2} e^{-(\sigma_r^2 - \sigma_s^2)k^2} \tag{10}$$

The plot of the algorithm of the amplitude versus k^2 yields a straight line. From the intercept and slope of this straight line the unknown coordination number and the relative value of the Debye–Waller factor ($\Delta\sigma^2$) can be determined.

When it is not possible to isolate a single shell EXAFS function in r-space, the above described amplitude ratio and phase comparison methods are not applicable. In such cases, a group of two or more shells is isolated and a nonlinear least square curve-fitting technique is applied. A function $\chi(k)$ is calculated using the reference amplitude and phase functions and the structural parameters are varied until the calculated function is in good agreement with the experimental data. The quality of the fit is checked both in the k-space

and in r-space. Also a single shell EXAFS function can be analysed using a non-linear least square fit.

The EXAFS function $\chi(k)$ shown in Figure 4(b) can also be analysed by carrying out a single-shell or multishell non-linear least square fit using the theoretically calculated $\phi_j(k)$ and $F_j(k)$ functions [11, 12]. In this case, the normalization is achieved by dividing through the tabulated values of μ_0 instead of dividing through the edge jump. Such an analysis requires knowledge of $\lambda(k)$ and S_0^2 as well as an initial guess of σ^2 for each shell.

In deriving equation (7) one assumes the presence of a Gaussian pair–distribution function and small disorder. If the pair–distribution function is not Gaussian and if the system is highly disordered, the standard data analysis procedure described here is not valid.

The reliability of the EXAFS analysis depends upon the transferability of the reference phase shift and amplitude functions [13]. Great care must be taken in selecting the reference compounds for providing the reference amplitude and phase functions. If theoretically calculated functions are used, they should be optimized by testing them on reference compounds. The accuracy of the structural parameters obtained from EXAFS analysis depends upon many factors such as the quality of the data, the length of the data range, the amount of disorder, the choice of the reference compound and the complexity of the system being studied. Typical accuracies are 1% for the determination of coordination distances, 10 to 20% for the coordination numbers and 10 to 20% for Debye–Waller factors.

3.2.4 Detection Methods

A variety of experimental set-ups have been designed so that XAFS experiments can be carried out *in situ* at high temperature and pressure and under influence of different gases [14, 15]. A standard experiment set-up to measure XAFS data consists of an X-ray source, a crystal monochromator, X-ray detectors, a sample stage and a data-aquisition system. Commonly a synchrotron storage ring is used as an X-ray source for most of the XAFS investigations. Typical data-collection times are 30 minutes when using a synchrotron source. Depending upon the nature of the sample and the information required one has to combine a suitable experimental set-up with a particular detection scheme.

The simplest and most widely used method is to measure the absorption (μx) of the sample in the transmission mode. Figure 5 shows the transmission XAFS measurement as used at beamline 9.2 of the Daresbury Synchrotron Radiation Source, UK. The monochromator is scanned through a desired energy range and the incident (I_0) and transmitted (I) X-ray intensities are recorded. The absorption is calculated using the relation $\mu x = \ln(I_0/I)$. Trans-

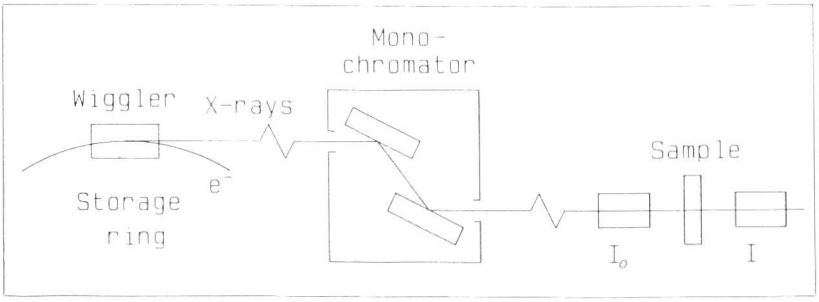

Figure 5 A transmission EXAFS experimental set-up as used at beamline 9.2 of the Synchrotron Radiation Source, Daresbury (UK). I_0 and I are ionization chambers to monitor the incident and transmitted X-ray intensities

mission XAFS measurements are suitable for concentrated and medium diluted samples (concentration > 100 mM).

Other detection schemes to measure XAFS involve monitoring secondary processes that are proportional to the basic absorption μx. Two such processes are the emission of X-ray fluorescence photons and Auger electrons [16]. The schematics of these processes are shown in Figure 6. Detection of fluorescence radiation gives better quality data than the transmission mode for dilute samples (concentration < 20 mM). The intensity of the fluorescence radiation (I_f) can be detected by ionization chambers, scintillation counters or solid-state detectors. The absorption is calculated by the relation $\mu x = I_f/I_0$.

Detection of Auger electrons requires ultra-high vacuum (UHV) environment. In electron detection mode, a strong surface sensitivity is achieved since the escape depth of electrons is <30 Å. Electron-detected EXAFS is known as SEXAFS (surface EXAFS) and it is used for studying adsorbates on surfaces [17]. SEXAFS experiments can be carried out by measuring the intensity of the elastic Auger electrons, scattered Auger electrons, secondary electrons or all the electrons emitted from the surface. Depending upon the various constituents of a sample, one can decide the applicable electron detection channel.

Electron-detected EXAFS can also be measured in helium atmosphere. The helium gas forms an ionization detector and the electron signal is significantly enhanced [18]. This method is suitable for interfacial investigations and offers near-surface sensitivity without requiring UHV environment.

A recent experimental set-up for studying interfaces and chemical reactions occurring on surfaces uses glancing incidence angle geometry shown in Figure 7 [19, 20]. At incidence angles lower than the critical angle, the X-rays undergo total external reflection and the X-ray penetration depth is only 20

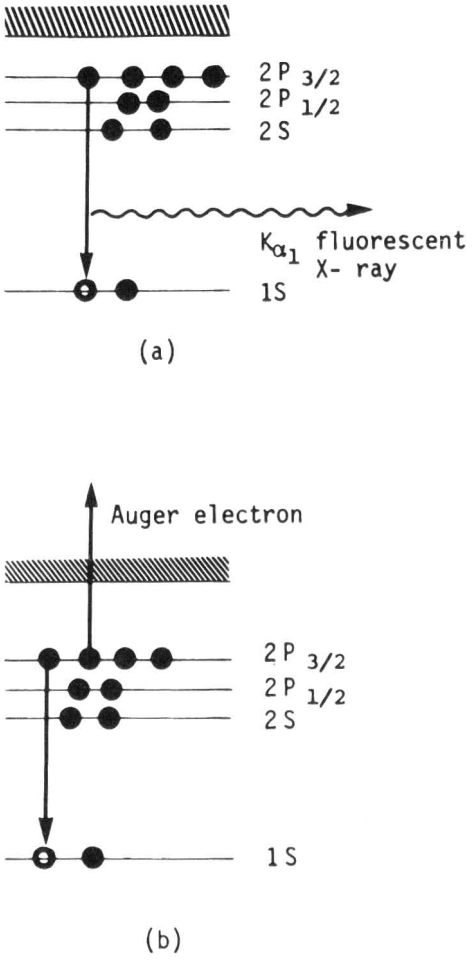

Figure 6 Schematic diagram of emission of (a) fluorescence photon and (b) Auger electron after the ejection of a photoelectron from the K shell

to 30 Å. By varying the incident angle, the penetration of the incident X-rays can be controlled to the interfacial region allowing solid/solid interfaces to be probed. The EXAFS signal is measured either by detecting the reflected X-rays or the fluorescence radiation. In contrast to SEXAFS, glancing-angle EXAFS offers surface sensitivity without requiring UHV environment. However, the glancing-angle reflected EXAFS data are distorted by the anomalous dispersion effects, and they must be corrected before using standard EXAFS data analysis procedures.

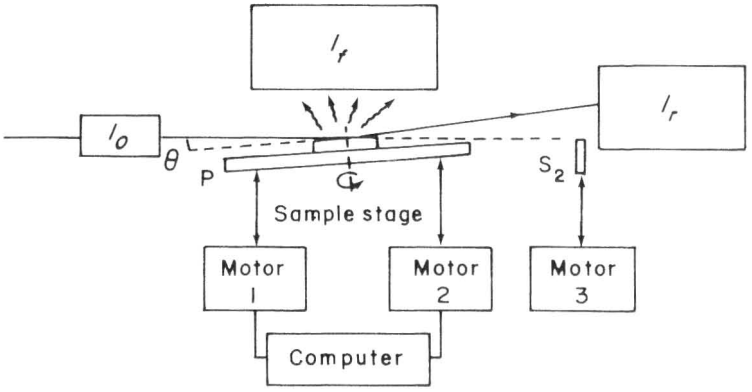

Figure 7 A glancing-angle experimental set-up. Sample is mounted on the platform P. Ionization chambers I_0, I_r and I_f record the intensities of the incident, reflected and fluorescent X-rays. θ is the angle of grazing incidence, which is controlled by stepper motors 1 and 2. Stepper motor 3 adjusts the intensity height I_r of the ionization chamber

3.2.5 Applications

In the past few years XAFS has been extensively used for characterizing disordered materials such as catalysts, metallic and oxide glasses, amorphous alloys, polymers, proteins and solutions. XAFS is a non-destructive technique which provides valuable information such as cluster growth, grain boundary interdiffusion and compound formation at the interface. In this section we give a few selected examples to illustrate the strength of this technique.

3.2.5.1 Solid/solid interface studies

The ability of the EXAFS technique for structural investigations of solid/solid interfaces is illustrated in the following examples, which are relevant for the electronic industry.

The first example describes a study of an Si_3N_4 layer deposited on a GaAs surface [21]. The Si_3N_4–GaAs system is used for MISFET components. The performance and the long-term stability of MISFET components strongly depend upon the Si_3N_4/GaAs interface layer. The Si_3N_4 layers were deposited by (a) reactive plasma treatment and by (b) a plasma-enhanced CVD process. The thickness of the Si_3N_4 overlayer was 175 Å for both samples. Previous XPS and REFLEX AFS experiments have shown that the chemical composition of the interface depends upon the method of preparation. Electron-detected EXAFS is a suitable technique to study such interfaces because it is capable of probing buried interfaces. Ga K-edge EXAFS experiments were carried out in the electron-detection mode in a helium atmosphere for crystal-

line GaAs and Si_3N_4–GaAs samples. The Fourier transforms of the EXAFS data obtained from the reactive plasma treated sample and from the plasma-enhanced CVD processed sample are shown in Figure 8(a) and (b), respectively. The major peaks in the Fourier transforms of both the samples are due to gallium atoms in GaAs. However, for the reactive plasma deposited sample, a shoulder is seen on the first peak of the Fourier transform (Figure 8a), which shows the presence of a GaN layer at the interface. Thus the reactive plasma deposited film is not suitable as an abrupt junction needed for MISFET components. This observation is in agreement with the XPS and REFLEX AFS results.

The second example describes a recent study of an Si/Ge/Si monolayer heterostructure on Si(1 0 0) prepared by MBE [22]. The heteroepitaxial growth of a Ge_xSi_{1-x}/Si strained layer superlattice on silicon substrates has interesting properties such as strain-induced optical transitions or two-dimensional transport properties. The lattice mismatch between bulk germanium and silicon is 4.2% which induces in-plane strain in the superlattice. The electronic states of the Ge_xSi_{1-x}/Si superlattice are sensitive to internal strains, and therefore it is important to study the lattice strain from microscopic viewpoints. Glancing-angle EXAFS is a surface-sensitive technique which probes not only the first few layers but also the region beneath the surface. Ge K-edge EXAFS data for crystalline germanium, Si/Ge/Si heterostructure and a-$Ge_{0.05}Si_{0.95}$:H samples were measured in glancing-angle geometry

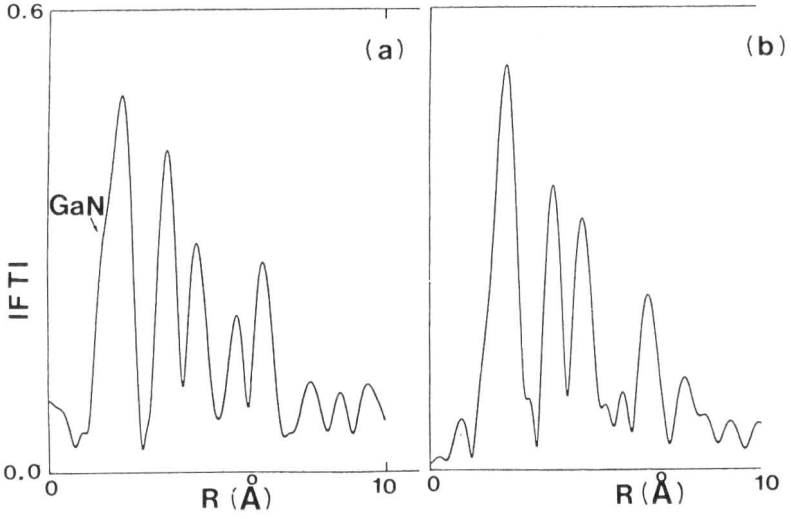

Figure 8 Fourier transform of EXAFS data for Si_3N_4–GaAs samples prepared by (a) reactive plasma treatment and (b) plasma-enhanced CVD process

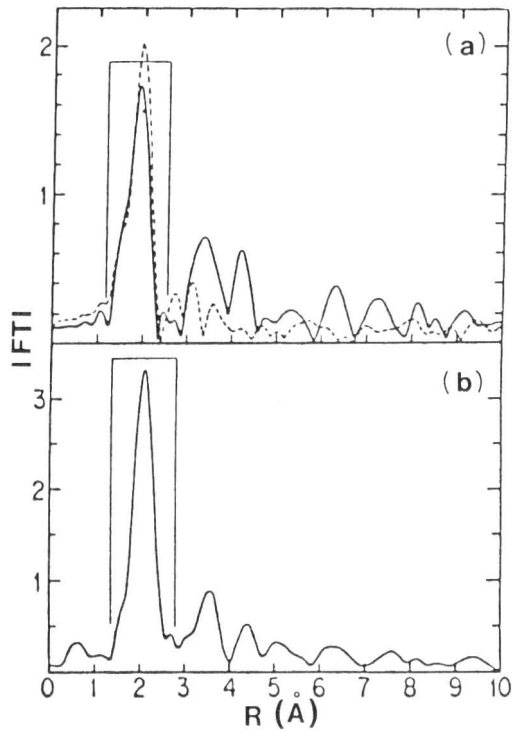

Figure 9 Fourier transform of EXAFS data for (a) Si/Ge/Si(100) monolayer heterostructure (solid line) and bulk a-$Ge_{0.05}Si_{0.95}$:H (dashed line) and (b) crystalline germanium

collecting the fluorescence radiation using a high-resolution solid-state detector. Figure 9(a) shows the Fourier transforms of the EXAFS data of the Si/Ge/Si(1 0 0) and $Ge_{0.05}Si_{0.95}$:H samples. The Fourier transform of the EXAFS data of crystalline germanium is given in Figure 9(b). The first prominent peak at 1.9 Å for the Si/Ge/Si heterostructure is attributed to the Ge–Si coordination shell. The peaks located at higher r values are due to the second and third nearest neighbours, and their presence indicates an ordered heterointerface. Detailed EXAFS analysis using theoretical phase shift and amplitude functions leads to the conclusion that (a) the germanium atoms are coordinated mostly with silicon atoms ruling out a possibility of formation of germanium clusters and (b) the Ge—Si bond distance is 2.38 Å for the Si/Ge/Si heterostructure and 2.40 Å for the $Ge_{0.05}Si_{0.95}$:H sample. The contraction of 0.02 Å in Ge—Si bond length for the Si/Ge/Si heterostructure as compared to bulk $Ge_{0.05}Si_{0.95}$:H reduces the bond length mismatch at the heterointerface to 1.3%. This suggests a large contribution of bond length relaxation at the heterointerface.

3.2.5.2 Determination of dopant environment in amorphous silicon

In contrast to crystalline silicon, the doping of amorphous silicon with Group III and Group V impurities is inefficient, since most of the impurities alloy with the matrix making electronically inactive sites. The active sites in amorphous silicon acquire tetrahedral coordination through charge exchange with dangling bond silicon atoms, making Group III negatively and Group V dopants positively charged [23].

Glancing-angle XAS has been used [24] to study gallium and arsenic implants (0.5%) in *n*-type amorphous silicon containing 3% phosphorus. The total external reflection geometry was used to match the X-ray penetration depths to the ion implantation depths (100 Å). A thirteen-element SSD detector measured the impurity fluorescence signal, windowing out the scatter from the silicon matrix. A good signal-to-noise ratio has been obtained for ion implementation dosage of 8×10^{15} down to 4×10^{14} atoms cm^{-2}. It was possible to determine the concentrations of the electronically active centres at the level of a few per cent for impurity loadings of 0.1 to 2%.

Changes in amplitudes between gallium and arsenic EXAFS spectra have been calibrated by directly comparing Fourier filtered data with the equivalent filtered data of substitutional arsenic (0.04 wt %) thermally grown in crystalline silicon. Applying the log-ratio method (equation 10) on the fine structure amplitudes for gallium and arsenic in amorphous silicon and for substitutional arsenic in crystalline silicon leads to the conclusion that more than one site has to be present (see Figure 10). Assuming an alloying site (A) and a tetrahedral site (B), the two can be deconvoluted. The intercept of B reveals that the fraction of tetrahedral sites is quite small (5 to 10%). The intercept of A gives the coordination number (N) of the dominating alloying site: for

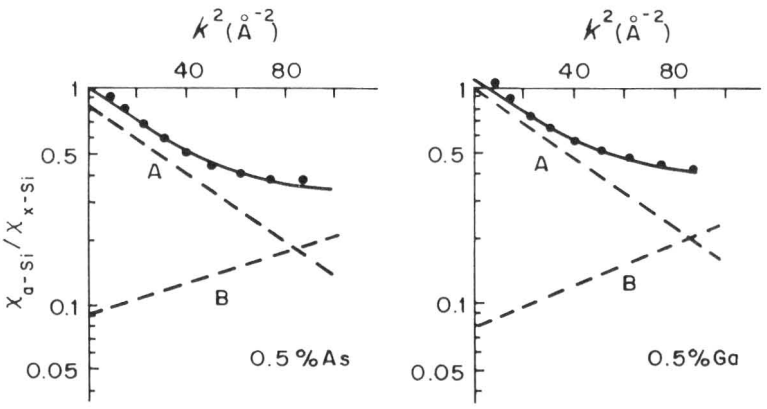

Figure 10 Log-ratio plot (solid line) and deconvolution (dotted lines) for 0.5% arsenic and 0.5% gallium implants in *n*-type amorphous silicon

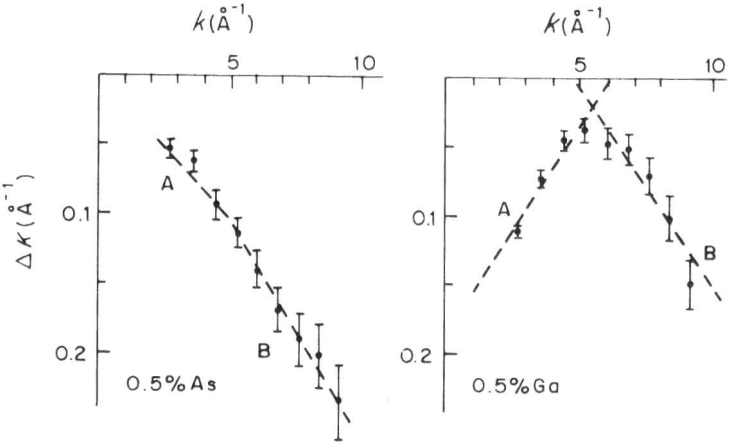

Figure 11 Differences in fine structure frequencies for 0.5% arsenic and 0.5% gallium implants in *n*-type amorphous silicon

gallium $N = 4.8$ and for arsenic $N = 3.5$. The slopes of the two contributions yield the differences in the Debye–Waller factor compared to the dopant in crystalline silicon. The alloying sites (A) (with a negative slope) are poorly ordered, whilst the tetrahedral sites (B) with a positive slope have a slightly better defined geometry compared to the crystalline state.

By comparing the fine structure frequency with that of arsenic in crystalline silicon (As–Si distance: 2.42 Å) it is possible to obtain the nearest neighbour distances for the alloying sites (A) (Ga–Si: 2.51 Å; As–Si: 2.37 Å) and for the tetrahedral sites (B) (Ga–Si: 2.29 Å; As–Si: 2.35 Å) (see Figure 11). The tetrahedral sites have substantially shorter distances in amorphous silicon compared to crystalline silicon, which also agrees with the better ordered local structure in amorphous silicon, as was found from the analysis of the EXAFS amplitudes. The detected shorter distances are consistent with Street's model [23], which predicts a charging of the tetrahedral sites in amorphous silicon.

Features of XAFS Spectroscopy

- Information about local structure (N, R and disorder)
- Local structure of each element constituting the sample can be probed selectively
- Application to crystalline, polycrystalline and amorphous samples
- Dopant detection limit 10^{15} atoms cm^{-2}
- Depth profiling using the glancing-angle XAS method for monolayer to 500 Å
- Most measurements can be performed *in situ*

References

1. P. A. Lee, L. H. Citrin, P. Eisenberger and B. M. Kincaid, *Rev. Mod. Phys.*, **53**, 769 (1981).
2. A. Bianconi, in *EXAFS and Near Edge Structure* (Eds. A. Bianconi, L. Incoccia and S. Stipcich), Springer-Verlag, Berlin (1983).
3. H. Bethe and E. Salpeter, *Quantum Mechanics of One and Two Systems*, Secs. 59 and 69, Springer-Verlag, Berlin (1957).
4. E. A. Stern, D. E. Sayers and F. W. Lytle, *Phys. Rev. B*, **11**, 4836 (1975).
5. C. A. Ashley and S. Doniach, *Phys. Rev. B*, **11**, 1279 (1975).
6. J. Wong, R. P. Messmeer, D. H. Maylotte and F. W. Lytle, *Phys. Rev. B*, **30**, 5596 (1984).
7. P. J. Durham, in *X-ray Absorption* (Eds. D. C. Koningsberger and R. Prins), Wiley, New York (1987).
8. J. B. A. D. van Zon, D. C. Koningsberger, H. F. J. van't Blik and D. E. Sayers, *J. Chem Phys.*, **81**, 5742 (1985).
9. D. E. Sayers and B. A. Bunker, in *X-ray Absorption* (Eds. D. C. Koningsberger and R. Prins), Wiley, New York (1987).
10. B. K. Teo, *EXAFS: Basic Principles and Data Analysis*, Springer-Verlag, Berlin (1986).
11. B. K. Teo, *J. Am. Chem. Soc.*, **103**, 3990 (1981).
12. A. G. McKale, B. W. Veal, A. P. Paulikas, S. K. Chan and G. S. Knapp, *J. Am. Chem. Soc.*, **110**, (12), 3763 (1988).
13. E. A. Stern, B. A. Bunker and S. M. Heald, *Phys. Rev. B*, **21**, 5521 (1980).
14. F. W. H. Kampers, T. M. J. Maas, J. van Grondelle, P. Brinkgreve and D. C. Koningsberger, *Rev. Sci. Instr.*, **60**, 2635 (1989).
15. R. Ingalls, E. D. Crozier, J. E. Whitemore, A. J. Seary and J. Tranquada, *J. Appl. Phys.*, **51**, 3158 (1980).
16. S. M. Heald, in *X-Ray Absorption* (Eds. D. C. Koningsberger and R. Prins), p. 87, Wiley, New York (1987).
17. J. Stohr, *Z. Phys. B*, **61** (1985).
18. K. I. Pandya, K. Y. Yang, R. W. Hoffman, W. E. O'Grady and D. E. Sayers, *J. de Phys.*, **C8**, 158 (1986).
19. S. M. Heald, J. M. Tranquada and H. Chen, *J. de Phys.*, **C8**, 825 (1986).
20. D. Jiang, N. Alberding, A. J. Seary and E. D. Crozier, *J. de Phys.*, **C8**, 861 (1986).
21. G. Tourillion, E. Dartyge, A. Fontaine, M. Lemonnier and F. Bartol, *Phys. Lett. A*, **121**, 251 (1987).
22. H. Oyanagi, T. Sakamoto, K. Sakamoto, T. Matsushita, T. Yao and T. Ishiguro, *J. Phys. Soc. Jap.*, **57 (6)**, 2086 (1988).
23. R. A. Street, *Phys. Rev. Lett.*, **49**, 1187 (1982).
24. G. N. Greaves, S. Kalbitzer, G. Kuller, S. Pizzini and K. J. Roberts, *Il Nuovo Cimento*, in press.